


Magnitude-intrinsic water–fat ambiguity can be resolved with multipeak fat modeling and a multipoint search method

Alexandre Triay Bagur  | Chloe Hutton | Benjamin Irving | Michael L. Gyngell |
Matthew D. Robson | Michael Brady

Perspectum Diagnostics Ltd, Oxford, United Kingdom

Correspondence

Alexandre Triay Bagur, Perspectum Diagnostics, 23–38 Hythe Bridge Street, Oxford, OX1 2ET, United Kingdom.
Email: Alexandre.Bagur@perspectum-diagnostics.com

Funding information

RADICAL has received funding from the European Union's Horizon 2020 research and innovation program under grant agreement no. 719445.

Purpose: To develop a postprocessing algorithm for multiecho chemical-shift encoded water–fat separation that estimates proton density fat fraction (PDFF) maps over the full dynamic range (0–100%) using multipeak fat modeling and multipoint search optimization. To assess its accuracy, reproducibility, and agreement with state-of-the-art complex-based methods, and to evaluate its robustness to artefacts in abdominal PDFF maps.

Methods: We introduce MAGO (MAGnitude-Only), a magnitude-based reconstruction that embodies multipeak liver fat spectral modeling and multipoint optimization, and which is compatible with asymmetric echo acquisitions. MAGO is assessed first for accuracy and reproducibility on publicly available phantom data. Then, MAGO is applied to $N = 178$ UK Biobank cases, in which its liver PDFF measures are compared using Bland-Altman analysis with those from a version of the hybrid iterative decomposition of water and fat with echo asymmetry and least squares estimation (IDEAL) algorithm, LiverMultiScan IDEAL (LMS IDEAL, Perspectum Diagnostics Ltd, Oxford, UK). Finally, MAGO is tested on a succession of high field challenging cases for which LMS IDEAL generated artefacts in the PDFF maps.

Results: Phantom data showed accurate, reproducible MAGO PDFF values across manufacturers, field strengths, and acquisition protocols. Moreover, we report excellent agreement between MAGO and LMS IDEAL for 6-echo, 1.5 tesla human acquisitions (bias = -0.02% PDFF, 95% confidence interval = $\pm 0.13\%$ PDFF). When tested on 12-echo, 3 tesla cases from different manufacturers, MAGO was shown to be more robust to artefacts compared to LMS IDEAL.

Conclusion: MAGO resolves the water–fat ambiguity over the entire fat fraction dynamic range without compromising accuracy, therefore enabling robust PDFF estimation where phase data is inaccessible or unreliable and complex-based and hybrid methods fail.

KEY WORDS

fat–water swap artefact, hepatic steatosis, magnitude-based water–fat separation, nonalcoholic fatty liver disease, phase error, proton density fat fraction

This is an open access article under the terms of the Creative Commons Attribution-NonCommercial License, which permits use, distribution and reproduction in any medium, provided the original work is properly cited and is not used for commercial purposes.

© 2019 The Authors. *Magnetic Resonance in Medicine* published by Wiley Periodicals, Inc. on behalf of International Society for Magnetic Resonance in Medicine

1 | INTRODUCTION

The increasing prevalence of nonalcoholic fatty liver disease and its progressive form, nonalcoholic steatohepatitis, necessitates the development of noninvasive quantitative biomarkers both to aid diagnosis and staging and to monitor therapy, including measuring the effectiveness of the anti-nonalcoholic steatohepatitis drugs under development.¹⁻⁴ Multiecho chemical-shift encoded (CSE) water-fat separation MRI methods are increasingly reliable and reproducible for complete fat suppression and for proton density fat fraction (PDFF) quantification.⁵⁻¹⁸ CSE methods exploit the differences in precession frequencies of water and fat to estimate fat content and have been validated against histological steatosis grading and spectroscopy measures.¹⁹⁻²⁴

To date, most CSE methods are complex-based in that they use both the magnitude and the phase of the MRI signal, and they calculate PDFF indirectly by first estimating a field map, which is a measure of (essentially inevitable) B_0 inhomogeneity.^{7,10,11,13,16,17,25-31} The water and fat contents at a voxel and their signal ratio PDFF may be uniquely determined provided that a field map value is available.²⁵ However, field map estimation is a nontrivial optimization problem, with multiple candidate solutions in the form of local minima. Convergence is sensitive to initialization and may lead to inaccurate water and fat measures, often with misidentification of the dominant species (*fat-water swap* artefacts).²⁵⁻²⁷ To mitigate this problem, a number of field map estimation algorithms use spatial regularization, although the implied smoothness may not hold in cases of poor shimming, local magnetic susceptibility (e.g., due to air-tissue interfaces), or hepatic iron overload,^{30,32} propagating errors. The Fat Likelihood Analysis for Multiecho Signals approach proposed using complementary information that results from fitting different signal models to potential field map solutions.³² Fat Likelihood Analysis for Multiecho Signals also exploited the spectral complexity of fat³³⁻³⁵ in complex-based water-fat separation to choose the appropriate field map solution based on residual values. However, the field map optimization space contains infinite minima and need not be periodic in the general case of asymmetric echoes. Furthermore, noise may corrupt the fitting residuals altering the global and local minima, leading to inaccurate PDFF estimates.

CSE methods assume that phase images are accessible and reliable. Although the former may be a reasonable assumption in a research setting,³⁶ it can be a challenge in routine clinical practice using particular scanner makes and models. This precludes the cross-vendor standardization of complex-based methods in clinical practice. Also, phase errors (e.g., due to eddy currents when the polarity of the readout gradient changes for alternating echo times) may clinically impact PDFF measures. For these reasons, magnitude-based methods (i.e., that only require magnitude

images) and hybrid methods have been proposed.^{15,17} Hybrid methods use a final magnitude-based estimation step to refine the PDFF values from phase errors but are still subject to field map estimation.^{17,37} Purely magnitude-based methods are not the first preferred option because they throw away complementary phase information that improves the SNR when phase data is available and error-free.³⁸ However, magnitude fitting is insensitive to phase errors and does not require prior field map estimation nor any related field map smoothness assumptions, enabling direct PDFF estimation. The adoption of magnitude methods has also been limited because of the reported inability to differentiate PDFF from 100% PDFF; this has been referred to as the *magnitude-intrinsic water-fat ambiguity*.^{3,15,17,32} In essence, fat-dominant pixels (e.g., subcutaneous fat regions in abdominal imaging) will be aliased to PDFF values below 50%, which could result in the following: 1) may mislead diagnosis when no other information about the body being imaged is available, and 2) could undermine the confidence of clinicians taking account of hepatic fat quantities. Furthermore, PDFF levels in the liver between 40% and 60% (although rare, these do occur) become ambiguous.

Bydder et al. suggested that the composite nature of the fat spectrum could help resolve the water-fat ambiguity retrospectively.^{15,39} In the particular case of in-phase/opposed-phase (IP/OP) echo acquisitions, Hernando et al. found that the ambiguity disappears using magnitude fitting of the IP echoes, provided that a fat model with multiple peaks is used.^{40,41} We show in this paper using simulations that this particular combination of acquisition and reconstruction is robust to small time shifts in echo sampling. However, there are known disadvantages of using IP/OP acquisitions, not least the noise performance and its dependence on PDFF; these are much less of a concern with asymmetric echoes.¹¹ Also, IP/OP acquisitions lead to poor SNR in the case of fast signal decay (e.g., due to hepatic iron overload) because only a small number of echoes correspond to signal as opposed to noise.^{40,42}

In this paper, we test whether a multipeak fat spectrum provides adequate information to unambiguously separate water and fat and resolve PDFF retrospectively across the entire 0 to 100% range in magnitude-based CSE-MRI with asymmetric echo times (not just IP/OP acquisitions). We show that the solution space of magnitude methods generally results in just 2 candidate PDFF solutions. We test whether multipoint search can correctly determine PDFF without compromising accuracy for a number of different acquisition protocols. The algorithm is validated using available phantom reproducibility data and then compared to a reference complex-based method in 178 healthy subjects. Furthermore, a set of challenging cases at high field strength are used to assess robustness and overall clinical performance.

2 | THEORY

A magnetic resonance signal s at a single voxel containing water, fat, and iron may be sampled at multiple echo times t_i during relaxation. For a general complex-valued signal, the following phase-constrained model may be used:

$$s[t_i] = \left(\rho_W + \rho_F \cdot \sum_{p=1}^P \alpha_p e^{j2\pi f_p t_i} \right) \cdot e^{j(2\pi\psi t_i + \phi_0)} \cdot e^{-R_2^* t_i}, \quad (1)$$

where ρ_W and ρ_F are real values for the unknown water and fat proton counts, respectively, and $R_2^* = 1/T_2^*$ (s^{-1}) is an unknown relaxation constant. The common phase term $\phi(t) = 2\pi\psi t + \phi_0$, where ψ is the unknown field map and ϕ_0

is the unknown phase offset at $t=0$ ⁴³; $j = \sqrt{-1}$. The term $\sum_{p=1}^P \alpha_p e^{j2\pi f_p t_i}$ is the fat spectral model comprising P peaks. In this formulation, α_p denotes the relative amplitude of the fat peak p with respect to the other fat peaks, and f_p is the difference in precession frequency of that fat peak p with respect to the water peak in Hz. It is usual practice to assume that the values $\{\alpha_p, f_p\}$ for all p are known empirically and constant throughout the image.^{16,35} PDFF may be calculated from the water and fat amounts using

$$\text{PDFF} = \frac{\rho_F}{\rho_W + \rho_F} \times 100 \text{ [\%]}. \quad (2)$$

When dealing with the magnitude of s , that is, $|s|$, the above model becomes:

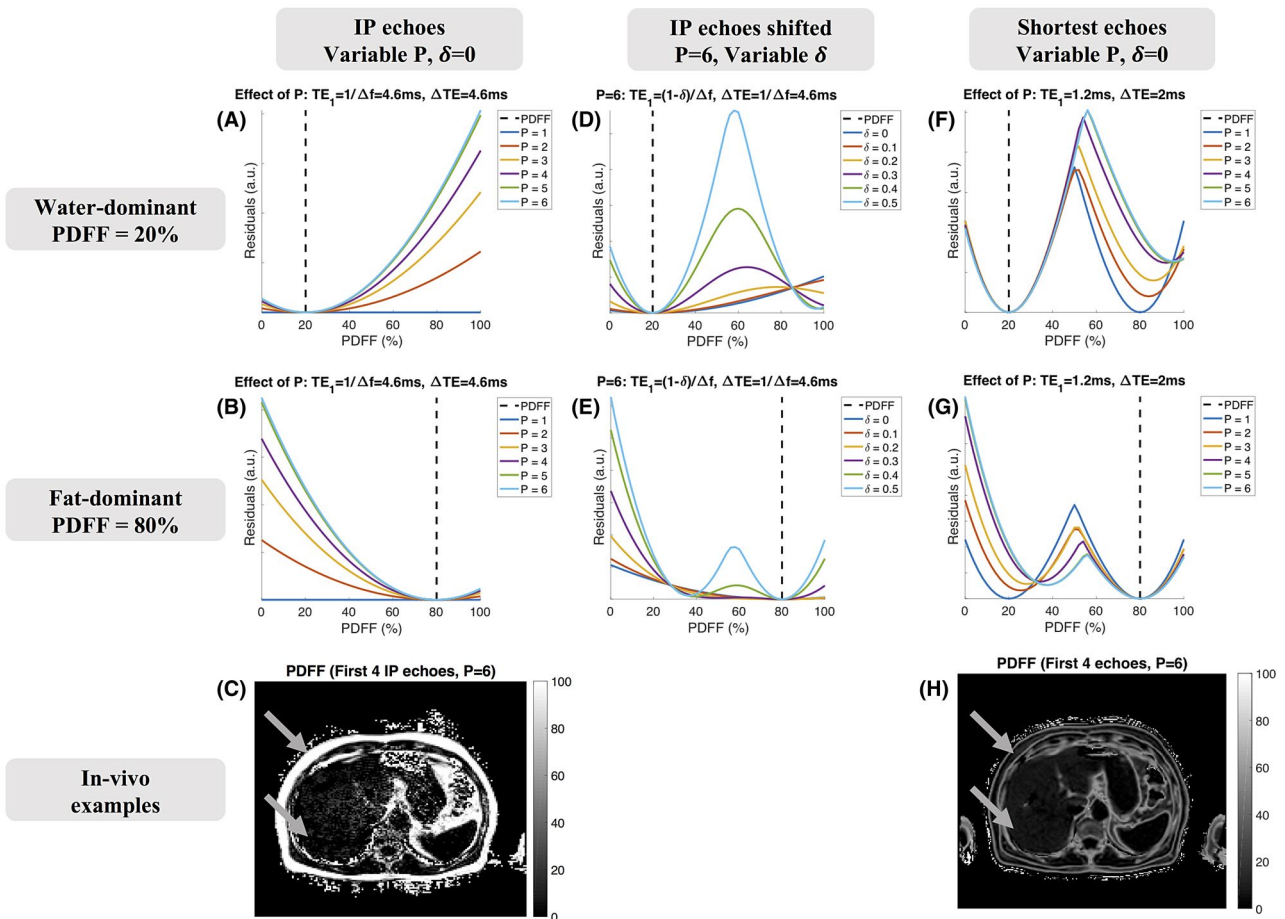


FIGURE 1 Illustration of the magnitude-intrinsic water-fat ambiguity with variable number of fat spectral peaks (P) and echo shifts (δ) using noise-free simulated data. In the single-peak model assumption with in-phase echo acquisition, that is, $P = 1$ and $\delta = 0$, the contributions of water and fat cannot be separated, and all PDFF values are equally valid solutions. Hernando and Reeder showed that if a more complete fat model is assumed, that is, $P \geq 2$, convergence to the correct solution is guaranteed for both water-dominant and fat-dominant pixels (A, B). The Hernando and Reeder reconstruction with multippeak fat modeling ($P = 6$) is shown to be robust to small echo shifts ($\delta \leq 0.2$) (D, E), but in the more general case of asymmetric echo times 2 minima will be present (F, G). Algorithms initialized near PDFF = 0% will converge to the correct solution for water-dominant pixels (F) and to the aliased solution for fat-dominant pixels (G); PDFF will be limited to a dynamic range of 0 to 50%. These residual plots were obtained as follows: for each combination of (P, δ), a 6-echo signal with true PDFF = 20% (A, D, F) or 80% (B, E, G) and fixed $R_2^* = 50 \text{ s}^{-1}$ was created; then 6-echo signals with the same (P, δ) and $R_2^* = 50 \text{ s}^{-1}$ but varying water and fat (thus PDFF) were generated, and the residual sum of squares between the true signal and generated signals were calculated for each PDFF value and shown. PDFF, proton density fat fraction

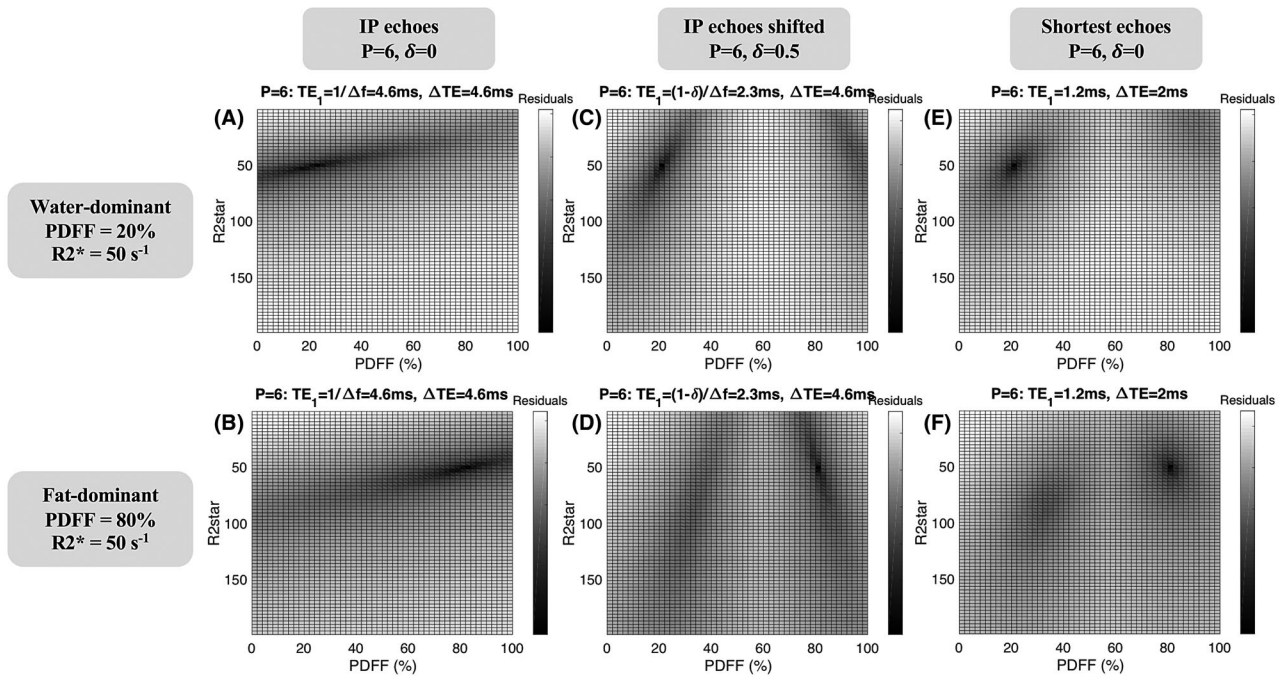


FIGURE 2 Illustration of the magnitude-intrinsic water–fat ambiguity with multiplex modeling ($P=6$) and variable echo shifts (δ) using noise-free simulated data over the physiological abdominal range of R_2^* values. Convergence to the correct solution is guaranteed for water-dominant and fat-dominant pixels when multiplex modeling is fitted to IP echo times (A, B). For a more flexible combination of echo times, an optimization algorithm initialized near PDFFF = 0% will converge to the correct solution of PDFFF and R_2^* for water-dominant pixels (C, E). The same optimization algorithm will converge to the local minimum for fat-dominant pixels, and its intensity will appear aliased to a value below 50% PDFFF (D, F). Note that there is no symmetry in the optimization space for an arbitrary combination of echoes and multiplex modeling: the aliased PDFFF, aPDFFF, will not be equal to 100%-tPDFFF, where tPDFFF is the true PDFFF value. Note the R_2^* from the local minimum will also be different to R_2^* from the global minimum. The RSS of the global minimum is lower than the RSS from the local minimum (C-F); by exploring the 2 solutions, the ambiguity may be resolved. IP, in phase; RSS, residual sum of squares

$$|s[t_i]| = \left| \rho_W + \rho_F \cdot \sum_{p=1}^P \alpha_p e^{j2\pi f_p t_i} \right| \cdot e^{-R_2^* t_i}. \quad (3)$$

For a single-peak fat spectral model ($P=1$) and an IP acquisition, that is, $\sum_{p=1}^P \alpha_p e^{j2\pi f_p t_i} = e^{j2\pi \Delta f t_i}$ and $t_i = i/\Delta f$ (with $i=1, 2, 3, \dots, N$; Δf is the frequency difference between the fat peak and the water peak in Hz), it may be shown that $|s_i| = |\rho_W + \rho_F| \cdot e^{-R_2^* t_i}$.⁴⁰ Evidently, the contributions of water and fat cannot be separated in this case (Figure 1A, B). As Hernando and Reeder showed for the same IP echo sampling but with the introduction of a multiplex fat model ($P \geq 2$), only the correct minimum remains; the magnitude-intrinsic ambiguity may be resolved (Figure 1A-C).⁴¹

For the multiplex fat model, for example with $P=6$, we may now move away from the IP acquisition by shifting the echo sampling by a known shift δ , that is, $t_i = (i - \delta)/\Delta f$. For example, $\delta=0.5$ corresponds to an OP acquisition. Whereas the Hernando and Reeder technique⁴¹ may be valid for non-zero δ , a local minimum appears for increasing δ (Figure 1D, E); in general, for a flexible combination of echo times, there are 2 minima in a broad range of physiological PDFFF and R_2^* (Figure 2E, B). Under such acquisitions, reconstruction

algorithms initialized near 0% PDFFF will converge to the correct solution for water-dominant voxels, but they will converge to the wrong estimates for fat-dominant voxels (Figure 1H). Magnitude methods previously described in the literature have consistently exhibited this behavior, with true PDFFF > 50% voxels aliased to estimates below 50%.^{15,17,37}

However, the magnitude-intrinsic water–fat ambiguity may be resolved with asymmetric echoes and multiplex fat modeling because the local minimum estimates will have higher fitting residuals than the global minimum estimates. The technique presented in this paper uses multipoint optimization to explore both minima and resolve the described ambiguity using a single signal model with a multiplex fat spectrum.

3 | METHODS

3.1 | Implementation

In this paper, we introduce a novel postprocessing algorithm for CSE-MRI based on multipoint search that we here refer to as MAGO (from MAGNitude-Only). The algorithm uses 2 or more applications of unconstrained nonlinear least-squares fitting, each starting from a different set of initial values. The cost function of the nonlinear least-squares optimization is

based on Equation 3, where the parameters ρ_W , ρ_F , and R_2^* are to be estimated, and the complex-valued vector referring to the multiplex fat model $\sum_{p=1}^P \alpha_p e^{i2\pi f_p t_i}$ is calculated a priori and used for all pixels during optimization.

To ensure that both minima are explored, the initial values of water and fat need to result in a low PDFFF in at least 1 run of the algorithm and to a high PDFFF in at least 1 other run. The initial value of R_2^* may be set to a physiologically occurring value in all runs. A given estimated parameter set (ρ_W, ρ_F, R_2^*) has an associated residual sum of squares (RSS) value in the form of the expression $RSS(\rho_W, \rho_F, R_2^*) = \sum_i^N (|\hat{s}_i| - |s_i|)^2$, where \hat{s}_i is the estimated signal using the estimated parameter set (ρ_W, ρ_F, R_2^*) in Equation 3, and s_i is the measured signal. The final solution at each voxel is chosen to be the parameter set with lowest RSS, although the other parameter sets may be retained as alternative solutions.

We implemented MAGO twice using variations of Levenberg-Marquardt optimization, the first using the *lsqcurvefit* function in MatLab R2017b (MathWorks, Natick, MA) and the second based on compiled C++ routines using The Insight Segmentation and Registration Toolkit (ITK) version 4.13.0 (www.itk.org). The results presented in this paper were generated using the second implementation, which enabled multithreaded processing and greater computational efficiency. In both implementations, the cost function gradient was calculated internally using default settings.

In both implementations, 2 parameter sets were obtained at each voxel from 2 different sets of initial values: $\{\rho_W, \rho_F, R_2^*\}_1 = \{1000, 0, 50s^{-1}\}$ in the first run and $\{\rho_W, \rho_F, R_2^*\}_2 = \{0, 1000, 50s^{-1}\}$ in the second run. The scaling of initial water and fat quantities was chosen empirically to account for different scanner gains across acquisitions. PDFFF maps for parameter set 1 and parameter set 2 were calculated with each parameter set using the converged water and fat amounts in Equation 2; $T_2^* = 1/R_2^*$ maps were also obtained. The solution at each voxel was chosen independently to be the parameter set with lowest RSS.

3.2 | Simulations

The feasibility of the MAGO technique was evaluated using simulations. For each PDFFF = 0 to 100% and SNR = 1 to 100, 1,024 signals (32×32 pixels) were generated using Equation 1 and sampled at the echo times of our in vivo protocols, which use the shortest echo times typically achievable across a range of different scanners: 1.5 tesla (T) simulations used 6 echoes ($TE_1 = 1.2$ ms, $\Delta TE = 2$ ms) and 3T simulations used 12 echoes ($TE_1 = 1.1$ ms, $\Delta TE = 1.1$ ms). Different levels of complex Gaussian noise were added to the signals depending on SNR. MAGO was applied to the magnitude images, and the median of the generated 32×32 MAGO PDFFF maps was compared against true PDFFF. The RSS difference between

the 2 converged parameter sets was extracted for each (PDFFF, SNR) pair. PDFFF from the 2 parameter sets were also plotted against true PDFFF for our typically observed SNR values in vivo (SNR = 40 at 1.5T and SNR = 60 at 3T).

Although the implementation referred to in this paper is pixel-independent in order to provide a baseline performance, the potential of using neighborhood information was explored in the simulations. The PDFFF solution image was thresholded at 60%, so 1 binary mask was obtained with pixels above 60% PDFFF and another with pixels at and below 60%. Small clusters (less than 50 pixels using 8-connectivity) were flagged, and the alternative parameter set was chosen as the solution at those pixels. Results with and without regularization were generated.

3.3 | Phantom data

MAGO was assessed using a publicly available dataset of 28 phantom acquisitions (<http://dx.doi.org/10.5281/zenodo.48266>).⁴⁴ In this dataset, a phantom comprising a total of 11 vials with peanut oil and water mixtures (PDFFF: 0%, 2.6%, 5.3%, 7.9%, 10.5%, 15.7%, 20.9%, 31.2%, 41.3%, 51.4%, 100%) was scanned at 6 different sites (2 Philips Healthcare, Best, the Netherlands, 2 Siemens Healthcare, Erlangen, Germany, and 2 GE Healthcare, Waukesha, WI, USA) using 2 different 6-echo gradient echo protocols (protocol 1 and protocol 2) at 2 field strengths (1.5T and 3T); 1 site acquired 2 sets of data ($(6+1) \times 2 \times 2 = 28$ acquisitions). Protocol 1 was an IP/OP acquisition ($TE_1 \approx \Delta TE \approx 2.30$ ms at 1.5T and $TE_1 \approx \Delta TE \approx 1.00$ ms at 3T), whereas protocol 2 aimed for the shortest possible echoes ($TE_1 = 1.10 - 1.20$ ms and $\Delta TE \approx 2.00$ ms at 1.5T, and $\Delta TE \approx 1.15$ ms at 3T). Acquisitions used a small flip angle ($2^\circ - 3^\circ$) to minimize T_1 bias and combined monopolar and bipolar readouts. The reader is referred to the original paper for further details regarding acquisitions.⁴⁴

Complex-valued datasets were available, but in order to assess MAGO, the phase information was discarded. The signal model used a 6-peak peanut oil fat spectrum corrected for a temperature of 22°C (frequencies in ppm of 5.20, 4.21, 2.66, 2.00, 1.20, and 0.80; relative amplitudes of 0.048, 0.039, 0.004, 0.128, 0.694, and 0.087).^{35,44,45} 15-mm diameter ROIs were placed manually by 1 author (C.H.) and used to extract a median value for each phantom vial from the central slice. Median PDFFF values were plotted against reference phantom concentrations, and linear regression was performed for comparison to the downloaded PDFFF maps, referred to as Hernando PDFFF. Linear regression was calculated independently for data from each field strength, protocol, and site.

3.4 | UK Biobank subjects

MAGO was evaluated for in vivo agreement with an independent, widely used method on $N = 178$ nominally healthy UK

Biobank⁴⁶ volunteers scanned at the Cheadle site (Siemens Healthcare, Magnetom Aera, 1.5T) using a single-slice (10-mm slice thickness), 6-echo ($TE_1 = 1.2$ ms, $\Delta TE \approx 2$ ms) gradient echo protocol designed to minimize T_1 bias (5° flip angle). UK Biobank is approved by the North West Multi-Centre Research Ethics Committee, and prior written consent was obtained from all participants. Magnitude and phase images were available for each case. PDFF maps were generated using MAGO applied to just the magnitude images and discarding phase information, and they were also generated using an implementation of the hybrid iterative decomposition of water and fat with echo asymmetry and least squares estimation (IDEAL) method¹⁷, LiverMultiScan IDEAL (LMS IDEAL, Perspectum Diagnostics Ltd, Oxford, UK), described in Hutton et al.³⁷ LMS IDEAL is a complex-based, confounder-corrected method that includes a region growing algorithm from Yu et al. for field map estimation and a final magnitude-based estimation step to mitigate phase errors.^{10,17,25} LMS IDEAL also includes a correction for bipolar gradients from Peterson and Månsson.⁴⁷

Both methods used an empirical human liver fat model described in the literature, with 6 peaks and frequencies in ppm of 5.30, 4.20, 2.75, 2.10, 1.30, and 0.90 ppm; and relative amplitudes 0.047, 0.039, 0.006, 0.12, 0.7, and 0.088, respectively.³⁵ For each case, a deep learning-based liver segmentation algorithm was used to obtain a mask with excluded vessels.⁴⁸ Liver masks were used to extract median PDFF values from the MAGO and LMS IDEAL PDFF maps. Median PDFF values were compared using Bland-Altman analysis.⁴⁹

3.5 | Challenging cases from the RADICAL project

MAGO was also applied to 3 particularly challenging cases from the project non-invasive rapid assessment of chronic liver disease using Magnetic Resonance Imaging with LiverMultiScan (RADICAL), in which artefacts were observed in LMS IDEAL PDFF maps. These cases had been acquired at 3 different sites at 3T: Leiden University Medical Center (Philips Healthcare, Ingenia, 3T), Coimbra University Hospital (Siemens Healthcare, TrioTim, 3T), and Ulm University Medical Center (Siemens Healthcare, Skyra, 3T) using 12 echoes, $TE_1 = 1.1$ ms, $\Delta TE \approx 1$ ms, 3° flip angle, and bipolar readouts. The Committee for Medical Ethics of Leiden University Medical Center (P17.076), the Committee of Ethics at the Faculty of Medicine of the University of Coimbra (CE-030/2017), and the Ethics Committee of the University of Ulm (Nr. 198/17) approved the study; and prior written consent was obtained from the participants. The chosen datasets contained multiple slices; off-center slices were processed for the Coimbra and Ulm cases to investigate the impact of larger off-resonance effects, which are usually

observed away from the isocenter. Liver segmentation masks were used to extract median hepatic measures and distributions of hepatic PDFF values.

4 | RESULTS

4.1 | Implementation

Figure 3 illustrates the intermediate steps of MAGO processing. The water-only, fat-only, and PDFF maps shown in Figure 3A through 3C were constructed with the converged parameter set 1 at each voxel; they show water-fat ambiguity similar to conventional magnitude-based reconstructions. On the other hand, the maps built with converged parameter set 2 at each voxel show the higher of the 2 possible PDFF minima (Figure 3E-G). PDFF 2 depicts infeasibly high hepatic PDFF, although subcutaneous fat and visceral fat are estimated in the expected range. Figure 3I through 3L show the result after selecting the parameter set corresponding to the lowest RSS at each voxel; this resolves the water-fat ambiguity.

4.2 | Simulations

Figure 4 shows the results of the MAGO reconstruction for the in vivo protocols with a range of SNR regimes. It is expected that, up to a given PDFF value, the PDFF from parameter set 1 will be chosen as the solution; above that PDFF value or *switching point*, the PDFF from parameter set 2 will be assigned instead. With multippeak fat modeling, the switching point need not be at 50% PDFF; in fact, it may be noted that it varies slightly with number of echoes and echo times. The switching point is approximately 58% PDFF in the current 1.5T and 3T protocols (Figure 4B). As PDFF approaches this value, the difference between residuals approaches 0, and there is increased ambiguity between the 2 candidate solutions (Figure 4A). In the presence of noise, a number of pixels may be incorrectly assigned, and the median PDFF value may become biased toward the alternative solution (Figure 4B, D). For a given number of echoes and echo times (e.g., our 3T protocol), it can be observed that PDFF 1 and PDFF 2 overlap for a short range of PDFF (Figure 4I); here, whereas the 2 parameter sets have the same residual value, choosing either of the 2 sets will give the correct solution (Figure 4F).

Figure 4 also shows the potential of using regularization in lower SNR conditions. For the 1.5T acquisition, the PDFF median becomes less biased toward the alternative solution when using neighborhood connectivity (Figure 4C). This substantially improves PDFF estimation about the switching point (Figure 4E). Neighborhood connectivity showed little improvement compared to pixel-independent assignment for the typical SNR observed in our 3T protocol (Figure 4H, J).

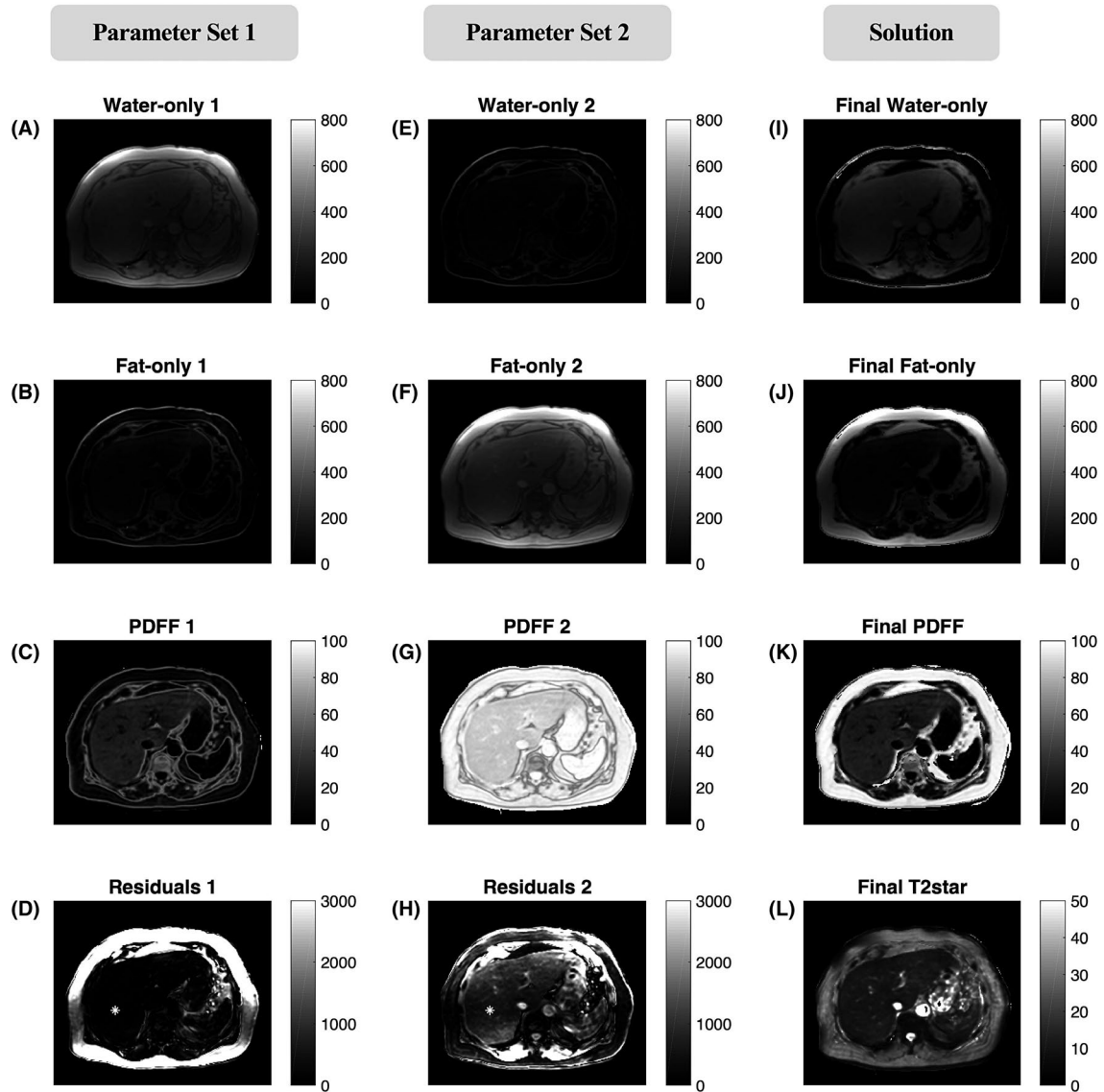


FIGURE 3 Intermediate solutions from the MAGO method implementation on a RADICAL case from the Ulm site (Siemens Healthcare, Erlangen, Germany, Skyra, 3T, 12 echoes, $TE_1 = 1.1$ ms, $\Delta TE \approx 1$ ms, 3° flip angle). One parameter set (ρ_W, ρ_F, R_2^*) will be obtained for each of the 2 runs of the optimization algorithm in each voxel, with 2 different sets of initial conditions $\{\rho_W, \rho_F, R_2^*\}_1 = \{1000, 0, 50\}$ and $\{\rho_W, \rho_F, R_2^*\}_2 = \{0, 1000, 50\}$ (water and fat amounts are in arbitrary units and R_2^* is measured in s^{-1}). The first set of initial conditions combines to PDFF = 0% and will lead to the parameter set 1 maps (A-D); this parameter set PDFF map (C) is similar to magnitude-based PDFF maps previously reported in the literature, where liver PDFF values are reported in the expected range, but subcutaneous and visceral PDFF values are aliased to values below 50%. The PDFF map of the parameter set 2 maps (E-H) has subcutaneous and visceral PDFF values in the expected range, but liver PDFF is infeasibly high. The solution water-only, fat-only, PDFF and T_2^* ($1/R_2^*$) maps (I-L) are constructed by choosing the parameter set (ρ_W, ρ_F, R_2^*) with lower RSS at each pixel. Residual values for the labeled pixel (marked *) were $R_1 = 51$ (J) and $R_2 = 510$ (K) in this case. This enables robust water-fat separation and quantification of PDFF within the entire dynamic range (0-100%). As may be noted, 2 spatially distant pixels with similar PDFF values could have substantially different RSS (see for example the subcutaneous fat in D); it is the relative difference between the RSS of the 2 parameter sets at each voxel that is evaluated. MAGO, MAGNitude-Only; RADICAL, non-invasive rapid assessment of chronic liver disease using Magnetic Resonance Imaging with LiverMultiScan; T, tesla

4.3 | Phantom data

Figure 5A shows a representative phantom acquisition with the PDFF map downloaded from Hernando et al.⁴⁴ and the PDFF map calculated using MAGO. The difference image shows excellent voxel-wise agreement between the methods and

similar noise performance, despite MAGO using only magnitude data. Figure 5B shows median PDFF values extracted from the ROIs placed on all 11 phantom vials, for all sites, acquisition protocols and field strengths plotted against reference phantom oil/water concentrations. Linear regression results are shown in Table 1 (slope, intercept, and R-squared

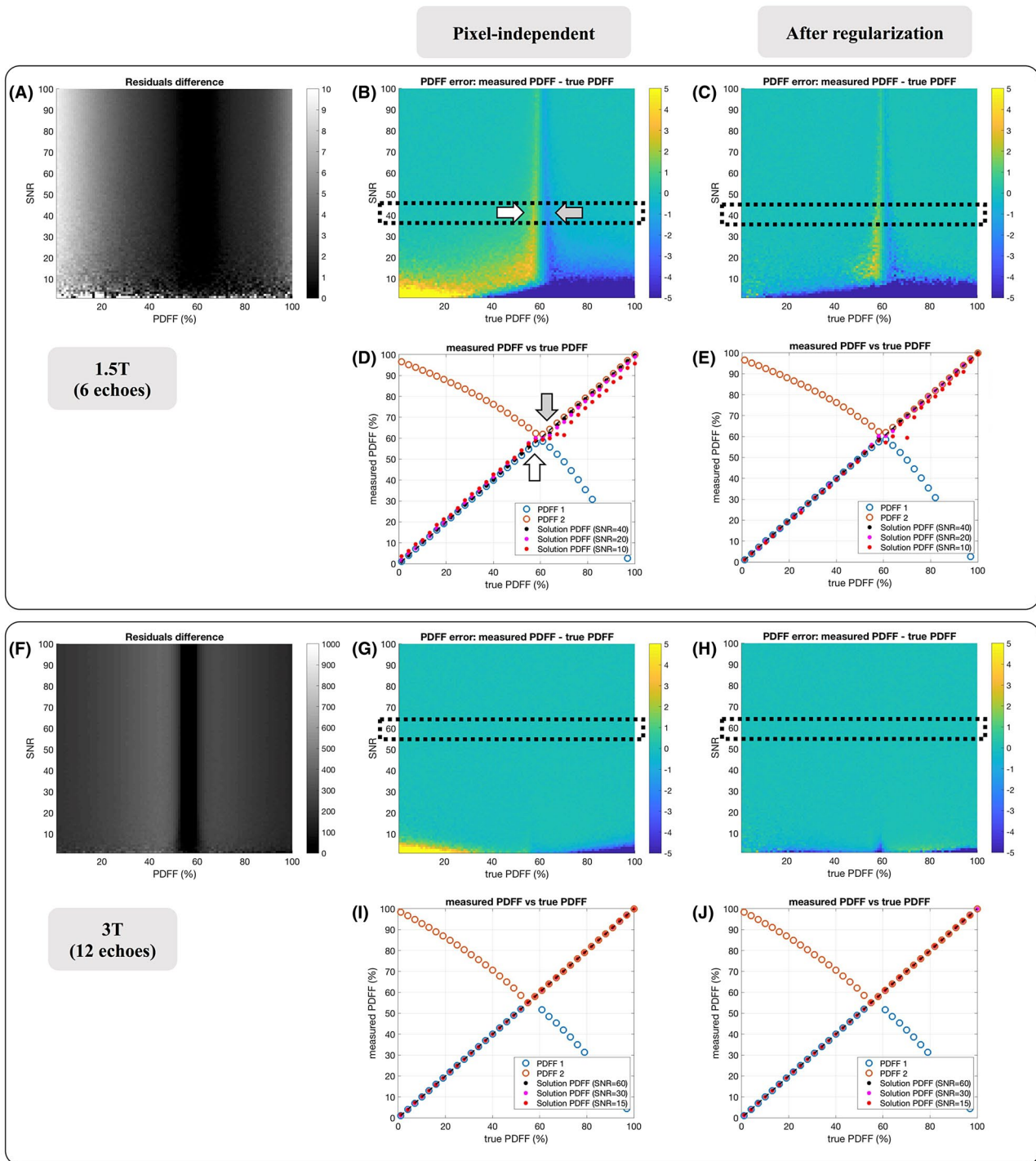


FIGURE 4 Noise simulations show the feasibility of the MAGO reconstruction technique in our preferred 1.5T and 3T acquisition settings for SNR = 1 to 100. The combination of the 2 candidate solutions or parameter sets (referred as PDFF 1 and PDFF 2) results in robust PDFF quantification over the entire range 0 to 100%. The 1.5T acquisition has less resolvability power than the 3T acquisition, shown by the difference in residual values (A, F), but is still able to assign most pixels to the correct solution down to low SNR (B, D, G, I). For low SNR, noise may start corrupting the residuals, and more pixels will be assigned to the incorrect solution (notably near the *switching point*, arrows, where there is the highest ambiguity) biasing the median PDFF value towards the incorrect solution (B, D). Using regularization reduced the bias of low SNR at 1.5T (C, E) but did not show significant improvement in high SNR 1.5T or in our 3T protocol (H, J). Black dotted squares show typical SNR values observed in our 1.5T (SNR = 40) and 3T (SNR = 60) acquisitions

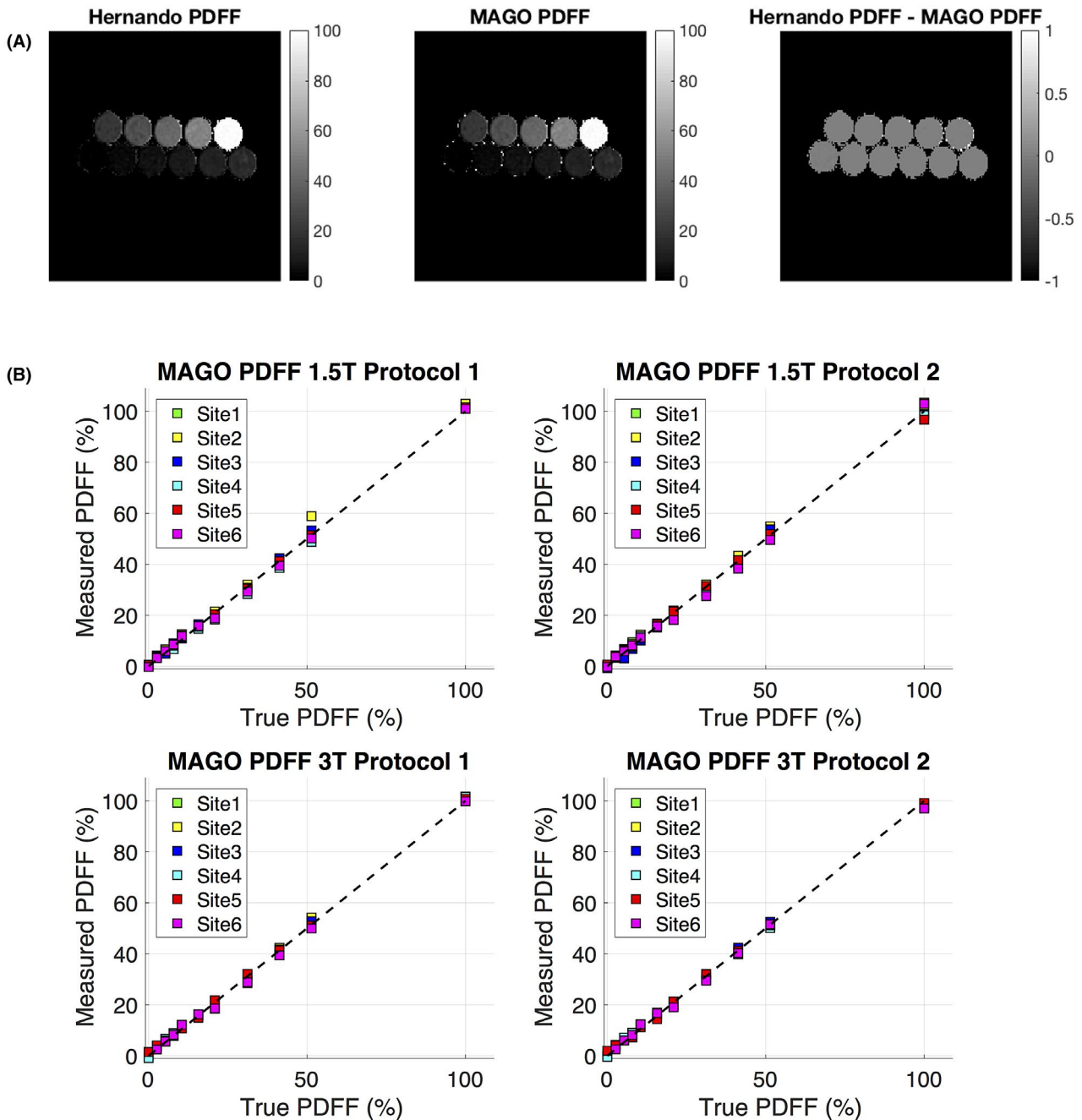


FIGURE 5 Results of MAGO applied on publicly available phantom data from Hernando et al.⁴⁰ Excellent pixel-by-pixel agreement is observed in the exemplary PDFF comparison taken from site 1, 3T, protocol 2 (note the tight scale of the difference image) (A). Reported values of MAGO PDFF from the phantom vials were plotted against ground truth concentrations for each site, field strength, and protocol; this plot may be used for qualitative assessment of accuracy, linearity, and bias (B). MAGO was able to resolve the magnitude-intrinsic water-fat ambiguity using magnitude images alone (note the vial containing 100% PDFF), and excellent reproducibility was observed across sites (manufacturers), protocols, and field strengths

agreement) and compares regression results from Hernando PDFF against MAGO PDFF. The results show excellent agreement between the methods, with high accuracy, high linearity, and small bias (note R-squared coefficients close to 1, slope close to 1, intercept close to 0). Note that MAGO is able to resolve the magnitude-intrinsic water-fat ambiguity;

this is mainly reflected in the 100% phantom vial results and does not compromise accuracy in the 0 to 50% PDFF range. In general, higher agreement between methods and between MAGO and ground truth values was observed on protocol 2 data over protocol 1 data and also on 3T data over 1.5T data.

TABLE 1 Linear regression analysis of MAGO median PDFF values on phantom vials was performed for all sites, protocols, and field strengths and was subsequently compared to the same analysis on the downloaded Hernando et al.⁴⁴ 2016 PDFF maps. Excellent agreement was observed between the 2 methods, with R^2 close to 1, slope close to 1, and intercept close to 0. Protocol 2 acquisitions presented better agreement than protocol 1 acquisitions because asymmetric echo acquisitions render greater noise performance than in-phase/opposed-phase acquisitions. Similarly, 3T acquisitions have higher SNR compared to 1.5T acquisitions, and better agreement was observed

MAGO PDFF 1.5T Protocol 1				Hernando PDFF 1.5T Protocol 1		
Site	R^2	Slope [95% CI]	Intercept [95% CI]	R^2	Slope [95% CI]	Intercept [95% CI]
1	0.999	1.00 [0.97 1.03]	0.41 [−0.67 1.48]	0.999	1.00 [0.97 1.02]	0.42 [−0.66 1.50]
2	0.997	1.04 [0.99 1.08]	0.81 [−0.93 2.55]	1	1.02 [1.00 1.03]	0.73 [0.15 1.32]
3	0.999	1.01 [0.99 1.03]	0.31 [−0.52 1.14]	0.999	1.01 [0.99 1.04]	0.33 [−0.55 1.22]
4	0.997	0.99 [0.95 1.04]	−0.57 [−2.27 1.13]	0.997	0.99 [0.95 1.04]	−0.55 [−2.24 1.14]
5	0.999	1.00 [0.99 1.02]	0.18 [−0.50 0.87]	0.999	1.01 [0.99 1.02]	0.21 [−0.46 0.88]
6	0.998	1.00 [0.96 1.03]	−0.15 [−1.37 1.06]	0.998	1.00 [0.96 1.03]	−0.14 [−1.34 1.07]
MAGO PDFF 1.5T Protocol 2				Hernando PDFF 1.5T Protocol 2		
Site	R^2	Slope [95% CI]	Intercept [95% CI]	R^2	Slope [95% CI]	Intercept [95% CI]
1	0.998	1.02 [0.99 1.06]	0.08 [−1.25 1.40]	0.998	1.02 [0.99 1.06]	0.09 [−1.21 1.39]
2	0.999	1.02 [1.00 1.04]	0.99 [0.28 1.71]	0.999	1.02 [1.00 1.04]	1.01 [0.29 1.74]
3	0.998	1.01 [0.97 1.04]	−0.38 [−1.58 0.82]	0.999	1.00 [0.98 1.03]	−0.39 [−1.46 0.68]
4	0.998	0.97 [0.94 1.00]	0.08 [−1.06 1.21]	0.998	0.97 [0.94 1.00]	0.09 [−1.04 1.21]
5	1	0.96 [0.95 0.98]	1.26 [0.68 1.84]	1	0.98 [0.96 0.99]	1.08 [0.67 1.50]
6	0.995	1.01 [0.96 1.06]	−0.74 [−2.72 1.25]	0.995	1.01 [0.96 1.06]	−0.71 [−2.69 1.26]
MAGO PDFF 3T Protocol 1				Hernando PDFF 3T Protocol 1		
Site	R^2	Slope [95% CI]	Intercept [95% CI]	R^2	Slope [95% CI]	Intercept [95% CI]
1	0.998	1.00 [0.97 1.03]	−0.03 [−1.20 1.14]	0.998	1.00 [0.97 1.03]	−0.01 [−1.17 1.15]
2	0.999	1.01 [0.99 1.03]	0.83 [0.11 1.55]	0.999	1.01 [0.99 1.03]	0.85 [0.12 1.58]
3	0.999	1.01 [0.99 1.03]	0.36 [−0.40 1.11]	0.999	1.01 [0.99 1.03]	0.38 [−0.38 1.13]
4	0.997	1.00 [0.96 1.04]	−0.13 [−1.71 1.44]	0.997	1.00 [0.96 1.04]	−0.12 [−1.68 1.45]
5	0.999	1.00 [0.98 1.01]	0.56 [−0.14 1.26]	0.999	1.00 [0.98 1.01]	0.57 [−0.12 1.26]
6	0.998	0.99 [0.96 1.02]	−0.45 [−1.74 0.84]	0.998	0.99 [0.96 1.02]	−0.43 [−1.71 0.85]
MAGO PDFF 3T Protocol 2				Hernando PDFF 3T Protocol 2		
Site	R^2	Slope [95% CI]	Intercept [95% CI]	R^2	Slope [95% CI]	Intercept [95% CI]
1	0.999	0.98 [0.96 1.00]	0.39 [−0.36 1.15]	0.999	0.98 [0.96 1.00]	0.40 [−0.34 1.15]
2	1	0.98 [0.97 0.99]	0.42 [−0.12 0.96]	1	0.98 [0.97 0.99]	0.43 [−0.11 0.97]
3	0.999	0.97 [0.95 1.00]	1.18 [0.12 2.24]	0.999	0.97 [0.95 1.00]	1.18 [0.15 2.21]
4	0.999	0.96 [0.94 0.99]	0.84 [−0.13 1.81]	0.999	0.96 [0.94 0.99]	0.84 [−0.13 1.82]
5	0.999	0.98 [0.96 1.00]	0.69 [−0.15 1.53]	0.999	0.98 [0.96 1.01]	0.61 [−0.25 1.48]
6	0.998	0.97 [0.94 1.00]	0.20 [−1.01 1.41]	0.998	0.97 [0.94 1.00]	0.20 [−1.00 1.41]

CI, confidence interval; MAGO, MAGNitude-Only; PDFF, proton density fat fraction; T, tesla.

4.4 | UK Biobank subjects

Figure 6A through 6C show an interesting UK Biobank case in which fat–water swapping occurred in the LMS IDEAL PDFF map affecting the arms and subcutaneous fat. The artefacts had no observable effect on liver PDFF because both methods reported a median PDFF of 4.9% and voxel-wise differences are small. Figure 6D shows the Bland-Altman analysis on the entire cohort ($N = 178$), namely a comparison between LMS IDEAL PDFF and MAGO PDFF median

values drawn from automatic liver segmentation masks. The Bland-Altman results show excellent in vivo agreement between LMS IDEAL and MAGO, with bias at -0.02% PDFF and 95% confidence intervals at $\pm 0.13\%$ PDFF.

4.5 | Challenging cases from the RADICAL project

Figure 7 shows a Leiden case in which LMS IDEAL presented substantial fat–water swap artefacts due to incorrect

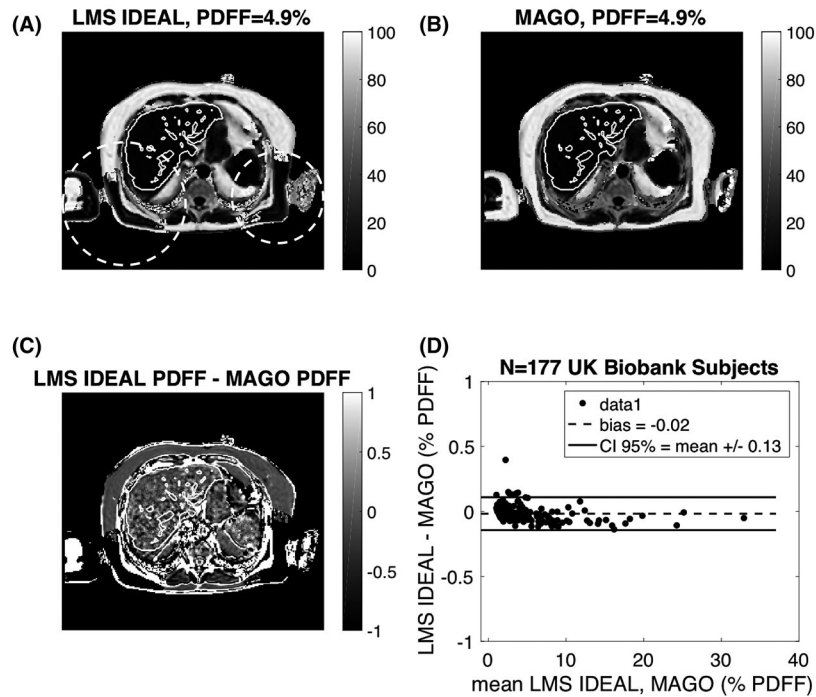


FIGURE 6 UK Biobank (Siemens Healthcare, Erlangen, Germany, Aera, 1.5T) results of reported segmentation median PDFF measures from the MAGO method against the reference state-of-the-art hybrid method LMS IDEAL (Perspectum Diagnostics Ltd, Oxford, UK). PDFF maps from an example where LMS IDEAL rendered fat–water swap artefacts (highlighted areas) are shown (A). The contour of automatic liver segmentation masks with excluded vessels are overlapped on the PDFF images (A, B) and the difference image (C). Pixel-wise agreement is observed in the difference image, notably within the liver mask; field map smoothness assumptions of LMS IDEAL cause apparent blurring of the LMS IDEAL PDFF map and salient borders in the difference image (C). Bland-Altman analysis comparing all $N = 178$ median PDFF measures from the 2 methods is included, with small bias and confidence intervals within clinical agreement ($-0.02\% \pm 0.13\%$ PDFF) (D). IDEAL, iterative decomposition of water and fat with echo asymmetry and least squares estimation; LMS, LiverMultiScan

field map estimation. Nonreliable phase data may have been caused by scanner-specific phase correction. The MAGO method appears robust to such errors and was able to resolve the magnitude-related water–fat ambiguity in all slices.

Figure 8 shows a Coimbra case in which LMS IDEAL had fat–water swapping in posterior subcutaneous fat. In homogeneously distributed liver fat cases, we would expect a normally distributed histogram of PDFF values around the median. Despite the agreement between the reported median PDFF values from the segmentation mask (11.2% PDFF in LMS IDEAL, 11.1% PDFF in MAGO), phase errors seem to propagate into the liver in LMS IDEAL maps because a noisier distribution is observed compared to MAGO (Figure 8E, F). Note that in many cases these errors are imperceptible when only evaluating the PDFF maps because of the scaling often given to these images combined with the fact that hepatic measures are rarely above 40% PDFF.

Figure 9 shows an Ulm case in which reported values between LMS IDEAL and MAGO differ considerably (9.4% PDFF in LMS IDEAL, 11.1% PDFF in MAGO). The histogram from the liver segmentations shows higher spread and a more flattened peak for LMS IDEAL than for MAGO (Figure 9E, F). Although the histogram suppresses spatial

information, increased local variation may be observed directly from the LMS IDEAL PDFF map (Figure 9B). Fat–water swapping is also observed in LMS IDEAL in anterior subcutaneous fat, whereas MAGO shows robustness in this region.

5 | DISCUSSION

This paper has introduced MAGO, a postprocessing algorithm for magnitude-based CSE-MRI that embodies a multipole fat spectrum and can use flexible echo combinations to estimate PDFF across the entire range (0–100%). Unlike field map estimation procedures, as used in complex-based CSE-MRI, for which the search algorithm has to contend with multiple local minima and for which an incorrect choice typically gives rise to fat–water swaps, we have shown that in general the magnitude-based CSE-MRI algorithms have to choose between just 2 local minima placed about approximately 50% PDFF. Using 6-echo phantom acquisitions and 6- and 12-echo human acquisitions, we have shown the feasibility of an implementation using as few as 2 runs of nonlinear least-squares optimization, 1 starting near 0% PDFF and the other near 100% PDFF, achieving robust determination of

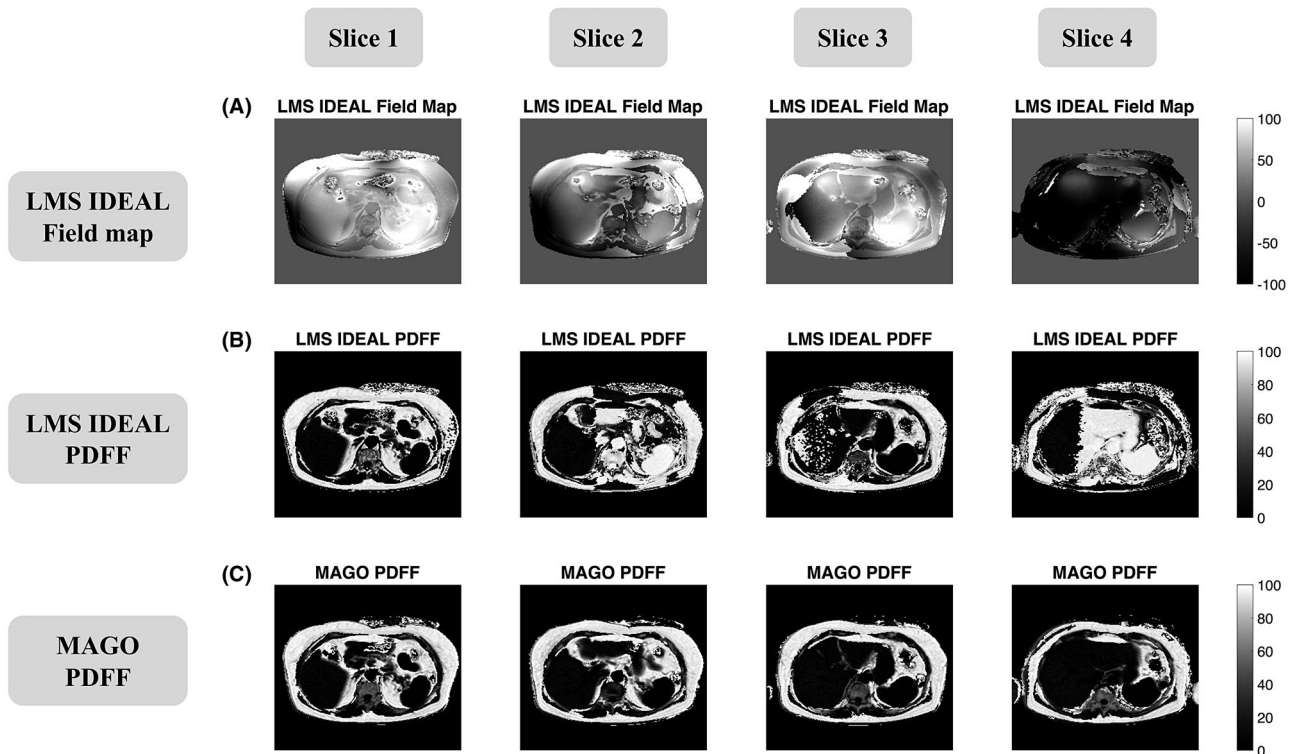


FIGURE 7 Results from a multislice RADICAL case (Philips Healthcare, Best, the Netherlands, Ingenia, 3T) show the effect of inconsistent phase information on field map estimation and subsequent PDFF maps calculation for the LMS IDEAL method. Field map convergence to local minima in certain regions (A) causes important fat–water swap artefacts in the LMS IDEAL PDFF maps that are propagated throughout the images (B), notably in the liver region and subcutaneous fat, but also in the spleen, spine, and descending aorta. MAGO PDFF maps show no evidence of fat–water swapping and are able to resolve the magnitude-intrinsic water–fat ambiguity over the entire PDFF dynamic range (0–100%) (C). A few MAGO PDFF pixels in the subcutaneous fat of slice 4 (C) were incorrectly assigned. We have seen this effect correlates to high signal loss due to susceptibility effects or RF inhomogeneity (results not shown), but further work is needed to confirm the association

the water and fat components. Whereas this paper has focused on PDFF, we note that MAGO also enables straightforward estimation of T_2^* ($1/R_2^*$), a surrogate for iron content. Although magnitude fitting of T_2^* as compared to complex fitting has to cope with *noise floor* effects that lead to T_2^* overestimation, techniques such as baseline fitting, signal truncation, or filtering could be used³⁰(p12).

We have shown from theory and simulated data that 3 necessary conditions are needed for resolved water–fat ambiguity: Condition 1 implies the use of magnitude fitting in order to reduce the multiple local minima from complex-based methods to generally 2. This makes the use of a search method more effective. Furthermore, convergence to local field map minima in complex fitting may not be readily apparent in PDFF maps because *double fat–water swaps* have been described in which reported PDFF values are incorrect but in the expected range²⁵(p3). In general, using magnitude fitting reduces the dimensionality of the search space and ensures that only 2 minima have to be explored, for which the appearance of potential incorrect convergence is more evident. Also, the use of magnitude fitting allows for direct estimation of water and fat (and therefore PDFF), without the need of a field map estimation step or typically used smoothness assumptions, which may not always hold.³⁰

Condition 2 involves the use of a multipole fat model in order to break the symmetry in the search space so that the 2 minima have different RSS and the ambiguity may be resolved. This is similar to the Fat Likelihood Analysis for Multiecho Signals approach³² but applied to magnitude-based reconstructions. Condition 3 is the use of a search space technique to explore the 2 minima. MAGO used multipoint search because knowledge about the search space is available, with 1 minimum below the switching point and another above. This ensures correct convergence when voxels are fat-dominant and prevents the convergence to local minima that has been observed in traditional magnitude-based techniques. We used Levenberg-Marquardt optimization, but other algorithms could be used at this stage.

Publicly available phantom data and PDFF results enabled comparison of MAGO to the implementation of IDEAL from Hernando et al.,⁴⁴ as well as accuracy assessment of MAGO against reference phantom values. Results show comparable performance of MAGO with respect to IDEAL in terms of slope, intercept, and R-squared agreement, as well as reproducibility for the full dynamic range of PDFF values. These reproducibility results suggest the potential of the MAGO reconstruction for in vivo standardization across scanner manufacturers, protocols, and field strengths.

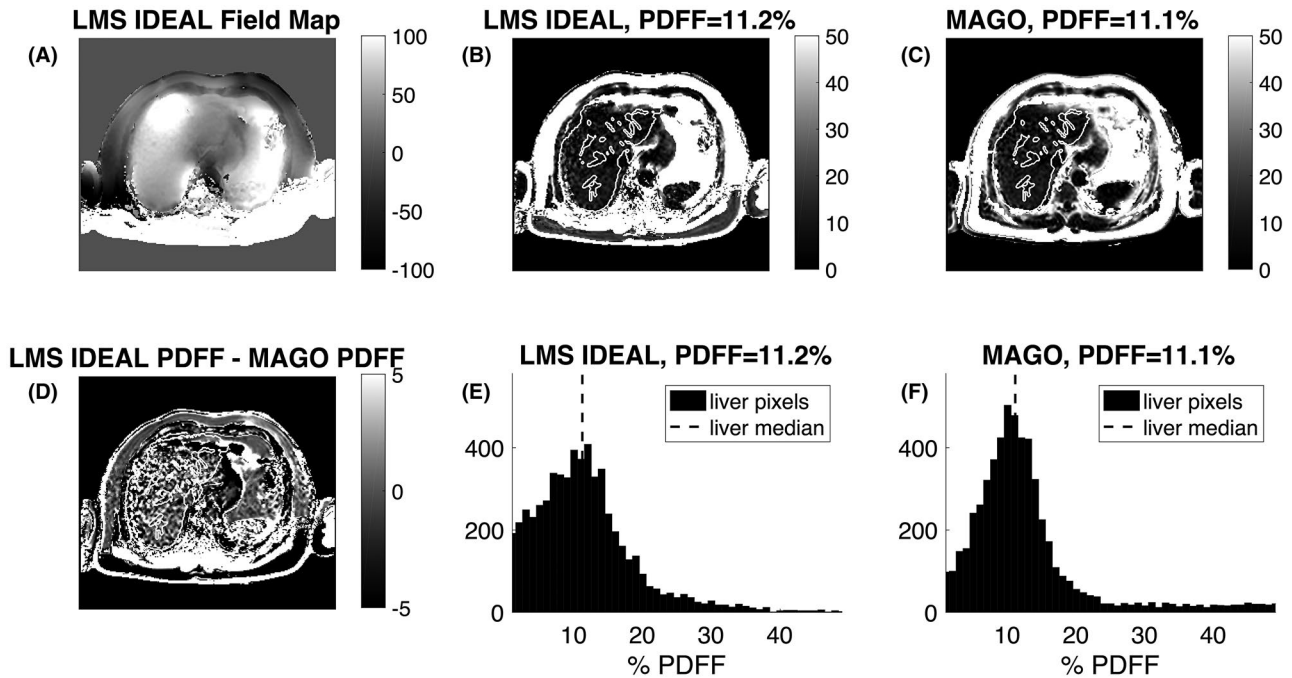


FIGURE 8 Results from a superior slice of a RADICAL case (Siemens Healthcare, Erlangen, Germany, TrioTim, 3T) show the effect of phase errors on the estimation of PDFF maps using LMS IDEAL and MAGO. The field map from LMS IDEAL (A) shows aliasing in the posterior area that reflects as a substantial fat–water swap artefact in the PDFF map (B), mainly affecting subcutaneous fat but also the spine, muscles, and left arm of the individual (right in the image). The MAGO PDFF map (C) shows no signs of fat–water swapping and resolves the magnitude-intrinsic water–fat ambiguity. Phase errors at a high field strength are reflected in the PDFF difference image (D) through a speckle pattern and a noisier distribution of LMS IDEAL PDFF values within the liver mask (E) compared to the MAGO distribution (F). The MAGO distribution seems to not go down to 0. Although we do not have an explanation for this phenomenon at this point, it is possible that this is due to the liver segmentation being fully automatic and including pixels in the noisy liver periphery that may give different estimates for the 2 reconstructions. The median LMS IDEAL PDFF value drawn from the liver segmentation is robust to the observed variability in this case, demonstrated by the reported PDFF measures of the 2 methods (LMS IDEAL PDFF = 11.2%, MAGO PDFF = 11.1%)

The observed inaccuracy in site 2 (Figure 5B) for the 51.4% phantom vial may be explained by the reported poor noise performance of magnitude fitting when water and fat exist in similar proportions.³⁸ With low SNR protocols, such as protocol 1 (IP/OP) at 1.5T (the lowest of the 4 combinations), noise may begin to confound—even dominate—the RSS differences, therefore affecting the identification of the correct solution. Thus, 6 echoes may not be sufficient to identify the correct solution. A possible approach to boost SNR could be to use phase information to weight the solution of a complex-based method more around 50%, similarly to hybrid reconstruction schemes.^{17,37}

The UK Biobank dataset ($N = 178$) was used for in vivo comparison of MAGO to LMS IDEAL, a hybrid reconstruction described in previous work.³⁷ The UK Biobank acquisitions were known to have reliable phase information and high overall quality despite the low field strength setting. The example case showed MAGO was able to resolve the magnitude-intrinsic water–fat ambiguity in the entire PDFF range 0 to 100% with improved robustness to fat–water swapping when LMS IDEAL maps had been affected. The excellent agreement between LMS IDEAL and MAGO reported PDFF

values using liver segmentations suggests that MAGO may be used alternatively to a complex-based method, even when phase information is accessible and predominantly error-free.

The RADICAL cases were used to evaluate the performance of the 2 methods in more challenging data acquired at 3T. MAGO presented higher robustness to fat–water swaps and other phase-related artefacts in these cases, whereas LMS IDEAL resulted in higher local variation in the liver compared to MAGO. This is notable given that LMS IDEAL includes a region-growing method that smooths the field map, whereas this version of MAGO was pixel-independent. The noisy local texture was not directly evident in the LMS IDEAL PDFF maps and, even for cases for which it does not clinically impact the median value of a segmentation (e.g., Figure 8), it could affect ROI-based measures more dramatically due to the sampling of a noisy distribution.

We have noted throughout the experiments that high-field MRI translates in MAGO to more robust and accurate PDFF estimates (e.g., see the simulations and RADICAL cases shown). This is a result of increased confidence in the difference of the RSS between the 2 explored solutions. This seems to be in contrast to complex fitting in 3T acquisitions

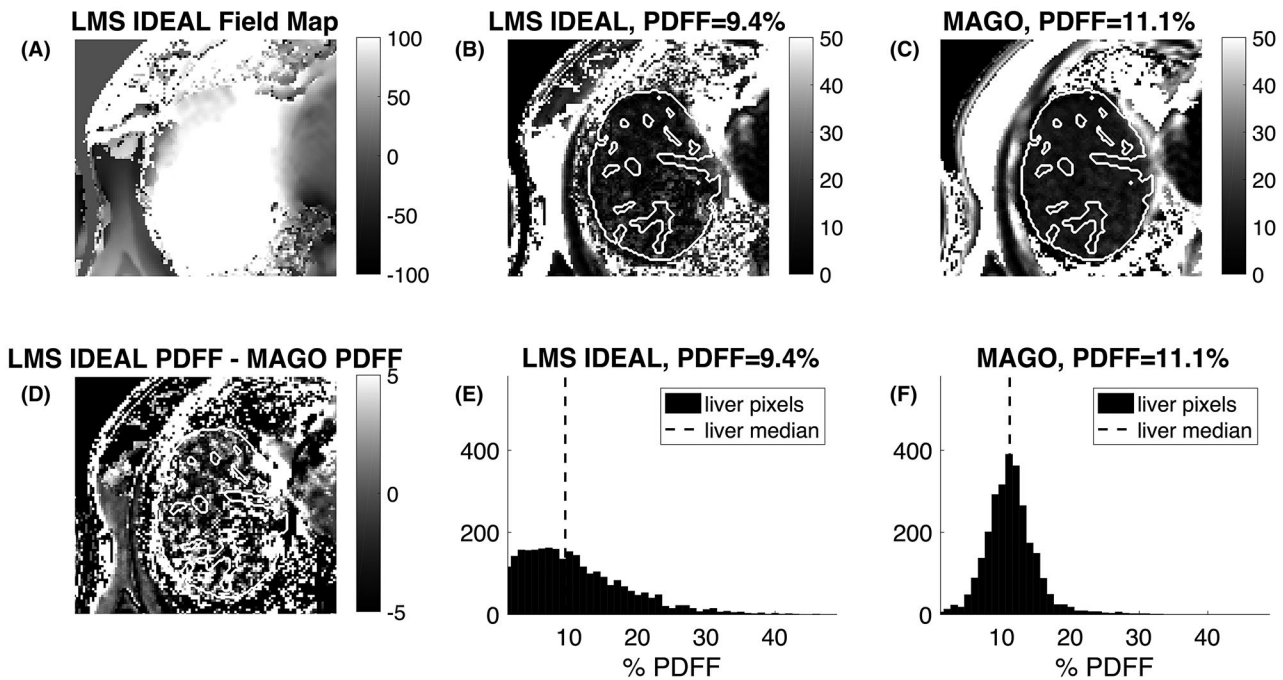


FIGURE 9 Results from a superior slice of a RADiCAL case (Siemens Healthcare, Erlangen, Germany, Skyra, 3T) show the impact of phase errors on reported PDFFF measures. Field map values from the LMS IDEAL method (A) cause a noisy pattern in the PDFFF map affecting the liver region (B). MAGO is unaffected by phase errors due to its magnitude-based nature and resolves PDFFF over the full dynamic range 0 to 100% (C). Plots have been rescaled to 0 to 50% to appreciate the local artefactual texture in the liver in LMS IDEAL that also shows in the difference image (D) and the histogram distributions of pixel intensities (E, F). Note that the 2 histogram distributions were drawn from the same automatic segmentation mask; the borders of the automatic segmentation mask were manually refined in this case. The segmentation median PDFFF reported values differ substantially (LMS IDEAL PDFFF = 9.4%, MAGO PDFFF = 11.1%)

for which the increase in SNR with respect to 1.5T comes at the cost of higher field inhomogeneities and more errors.

MAGO can be further developed in a number of ways. First, although it has been tested with a series of increasingly accurate human models (2–6 peaks) and a peanut oil phantom model, several additional models could be more thoroughly evaluated, not least the effect of temperature on the local minima.⁴⁵ Second, although it is well known that bipolar readout gradients affect complex-based images, they also impact magnitude images, albeit to a lesser extent.^{47,51} Adding correction for bipolar gradients causes more variables to be estimated, potentially decreasing SNR. This may be another reason for poorer performance of LMS IDEAL at 3T. Methods could be developed to compensate for bipolar gradients and to further increase SNR. It is also worth noting that our protocols use the shortest echo times typically achievable across a range of different scanners. Noise performance of our approach may be further improved using optimized echo times.

Spatial regularization could be used in association with MAGO. Simulations showed the potential increase in performance and reduced bias when spatial information is used to assign the solutions. The region growing algorithm of LMS IDEAL can result in over-smoothing of anatomical boundaries, which was reflected in the LMS IDEAL PDFFF–MAGO PDFFF difference images. Evidently, a more sophisticated

regularizer could be included during MAGO fitting (e.g., based on Markov Random Fields), respecting anatomical boundaries and other sharp transitions of PDFFF.

6 | CONCLUSION

The reconstruction algorithm introduced in this paper generally resolves the magnitude-related water–fat ambiguity by using a multippeak fat spectrum and a multipoint search approach. Multivendor, cross-field strength phantom data acquired with different protocols were used to validate the approach against reference values and demonstrated excellent reproducibility and agreement with complex-based methods in the literature. In vivo data from the UK Biobank study, which had known history of high-quality data, were used to compare the reported PDFFF from MAGO to a state-of-the-art hybrid reconstruction method, LMS IDEAL. No clinically relevant differences were observed between methods. MAGO showed excellent performance and improved robustness to fat–water swap artefacts on a range of challenging clinical cases, notably at high field strengths. The magnitude-based nature of MAGO extends the usability of advanced CSE-MRI in the clinic and contributes toward the development of robust standardized methods for the noninvasive quantification of fat.

ACKNOWLEDGMENT

This research has been conducted using the UK Biobank Resource under application 9914, and access to these data was facilitated by Steve Garratt, UK Biobank, Stockport, UK, and Jimmy Bell, University of Westminster, London, UK.

We also acknowledge the 3 clinical centers that are part of the RADICAL 1 project and that contributed data used in this manuscript: Leiden University Medical Center, Ulm University Medical Center, and Coimbra University Hospital. RADICAL has received funding from the European Union's Horizon 2020 research and innovation program under grant agreement no. 719445.

This publication is our view, and the Executive Agency for Small and Medium-sized Enterprises is not responsible for any use of the information herein.

CONFLICT OF INTEREST

Perspectum Diagnostics employees: Chloe Hutton, Michael L. Gyngell, Benjamin Irving, Alexandre Triay Bagur, Michael Brady; Perspectum Diagnostics stockholders: Alexandre Triay Bagur, Chloe Hutton, Michael L. Gyngell, Benjamin Irving, Matthew D. Robson, Michael Brady.

ORCID

Alexandre Triay Bagur  <https://orcid.org/0000-0002-5836-737X>

REFERENCES

1. Younossi ZM, Koenig AB, Abdelatif D, Fazel Y, Henry L, Wymer M. Global epidemiology of nonalcoholic fatty liver disease-Meta-analytic assessment of prevalence, incidence, and outcomes. *Hepatology*. 2016;64:73–84.
2. Williams CD, Stengel J, Asike MI, et al. Prevalence of nonalcoholic fatty liver disease and nonalcoholic steatohepatitis among a largely middle-aged population utilizing ultrasound and liver biopsy: a prospective study. *Gastroenterology*. 2011;140:124–131.
3. Caussy C, Reeder SB, Sirlin CB, Loomba R. Non-invasive, quantitative assessment of liver fat by MRI-PDFF as an endpoint in NASH trials. *Hepatology*. 2018;68:763–772.
4. Szczepaniak LS, Nurenberg P, Leonard D, et al. Magnetic resonance spectroscopy to measure hepatic triglyceride content: prevalence of hepatic steatosis in the general population. *Am J Physiol Endocrinol Metab*. 2005;288:E462–E468.
5. Dixon W. Simple proton spectroscopic imaging. *Radiology*. 1984;153:189–194.
6. Glover G. Multipoint Dixon technique for water and fat proton and susceptibility imaging. *J Magn Reson Imaging*. 1991;1:521–530.
7. Glover GH, Schneider E. Three-point Dixon technique for true water/fat decomposition with B0 inhomogeneity correction. *Magn Reson Med*. 1991;18:371–383.
8. Xiang QS, An L. Water-fat imaging with direct phase encoding. *J Magn Reson Imaging*. 1997;7:1002–1015.
9. Ma J, Singh SK, Kumar AJ, Leeds NE, Broemeling LD. Method for efficient fast spin echo Dixon imaging. *Magn Reson Med*. 2002;48:1021–1027.
10. Reeder SB, Wen Z, Yu H, et al. Multicoil Dixon chemical species separation with an iterative least-squares estimation method. *Magn Reson Med*. 2004;51:135–145.
11. Reeder SB, Pineda AR, Wen Z, et al. Iterative decomposition of water and fat with echo asymmetry and least-squares estimation (IDEAL): application with fast spin-echo imaging. *Magn Reson Med*. 2005;54:636–644.
12. Hussain HK, Chenevert TL, Londy FJ, et al. Hepatic fat fraction: MR imaging for quantitative measurement and display—early experience. *Radiology*. 2005;237:1048–1055.
13. Yu H, McKenzie CA, Shimakawa A, et al. Multiecho reconstruction for simultaneous water-fat decomposition and T2* estimation. *J Magn Reson Imaging*. 2007;26:1153–1161.
14. Liu CY, McKenzie CA, Yu H, Brittain JH, Reeder SB. Fat quantification with IDEAL gradient echo imaging: correction of bias from T(1) and noise. *Magn Reson Med*. 2007;58:354–364.
15. Bydder M, Yokoo T, Hamilton G, et al. Relaxation effects in the quantification of fat using gradient echo imaging. *Magn Reson Imaging*. 2008;26:347–359.
16. Yu H, Shimakawa A, McKenzie CA, Brodsky E, Brittain JH, Reeder SB. Multiecho water-fat separation and simultaneous R2* estimation with multifrequency fat spectrum modeling. *Magn Reson Med*. 2008;60:1122–1134.
17. Yu H, Shimakawa A, Hines CD, et al. Combination of complex-based and magnitude-based multiecho water-fat separation for accurate quantification of fat-fraction. *Magn Reson Med*. 2011;66:199–206.
18. Hines CD, Frydrychowicz A, Hamilton G, et al. T(1) Independent, T(2)(*) corrected chemical shift based fat-water separation with multi-peak fat spectral modeling is an accurate and precise measure of hepatic steatosis. *J Magn Reson Imaging*. 2011;33:873–881.
19. Cassidy FH, Yokoo T, Aganovic L, et al. Fatty liver disease: MR imaging techniques for the detection and quantification of liver steatosis. *Radiographics*. 2009;29:231–260.
20. Bley TA, Wieben O, François CJ, Brittain JH, Reeder SB. Fat and water magnetic resonance imaging. *J Magn Reson Imaging*. 2010;31:4–18.
21. Haufe WM, Wolfson T, Hooker CA, et al. Accuracy of PDFF estimation by magnitude-based and complex-based MRI in children with MR spectroscopy as a reference. *J Magn Reson Imaging*. 2017;46:1641–1647.
22. Nouredin M, Lam J, Peterson MR, et al. Utility of magnetic resonance imaging versus histology for quantifying changes in liver fat in nonalcoholic fatty liver disease trials. *Hepatology*. 2013;58:1930–1940.
23. Tyagi A, Yeganeh O, Levin Y, et al. inter-examination repeatability of magnetic resonance spectroscopy, magnitude-based MRI, and complex-based MRI for estimation of hepatic proton density fat fraction in overweight and obese children and adults. *Abdom Imaging*. 2015;40:3070–3077.
24. Yokoo T, Bydder M, Hamilton G, et al. Nonalcoholic fatty liver disease: diagnostic and fat-grading accuracy of low-flip-angle multiecho gradient-recalled-echo MR imaging. *Radiology*. 2009;251:67–76.

25. Yu H, Reeder SB, Shimakawa A, Brittain JH, Pelc NJ. Field map estimation with a region growing scheme for iterative 3-point water-fat decomposition. *Magn Reson Med*. 2005;54:1032–1039.
26. Hernando D, Haldar JP, Sutton BP, Ma J, Kellman P, Liang ZP. Joint estimation of water/fat images and field inhomogeneity map. *Magn Reson Med*. 2008;59:571–580.
27. Hernando D, Kellman P, Haldar JP, Liang Z-P. Robust water/fat separation in the presence of large field inhomogeneities using a graph cut algorithm. *Magn Reson Med*. 2010;63:79–90.
28. Lu W, Hargreaves BA. Multiresolution field map estimation using golden section search for water-fat separation. *Magn Reson Med*. 2008;60:236–244.
29. Lu W, Lu Y. JIGSAW: Joint inhomogeneity estimation via global segment assembly for water-fat separation. *IEEE Trans Med Imaging*. 2011;30:1417–1426.
30. Soliman AS, Yuan J, Vigen KK, White JA, Peters TM, McKenzie CA. Max-IDEAL: a max-flow based approach for IDEAL water/fat separation. *Magn Reson Med*. 2014;72:510–521.
31. Sharma SD, Artz NS, Hernando D, Horng DE, Reeder SB. Improving chemical shift encoded water-fat separation using object-based information of the magnetic field inhomogeneity. *Magn Reson Med*. 2015;73:597–604.
32. Yu H, Reeder SB, Shimakawa A, McKenzie CA, Brittain JH. Robust multipoint water-fat separation using fat likelihood analysis. *Magn Reson Med*. 2012;67:1065–1076.
33. Thomsen C, Becker U, Winkler K, Christoffersen P, Jensen M, Henriksen O. Quantification of liver fat using magnetic resonance spectroscopy. *Magn Reson Imaging*. 1994;12:487–495.
34. Szczepaniak LS, Babcock EE, Schick F, et al. Measurement of intracellular triglyceride stores by ¹H spectroscopy: validation in vivo. *Am J Physiol*. 1999;276:E977–E989.
35. Hamilton G, Yokoo T, Bydder M, et al. In vivo characterization of the liver fat ¹H MR spectrum. *NMR Biomed*. 2011;24:784–790.
36. Hernando D, Liang ZP, Kellman P. Chemical shift-based water/fat separation: a comparison of signal models. *Magn Reson Med*. 2010;64:811–822.
37. Hutton C, Gyngell ML, Milanese M, Bagur A, Brady M. Validation of a standardized MRI method for liver fat and T2* quantification. *PLoS ONE*. 2018;13:e0204175.
38. Hernando D, Hines CD, Yu H, Reeder SB. Addressing phase errors in fat-water imaging using a mixed magnitude/complex fitting method. *Magn Reson Med*. 2012;67:638–644.
39. Bydder M, Hamilton G, Yokoo T, Middleton MS, Chavez AD, Sirlin C. Fat-fat interactions in Dixon-variant imaging. In Proceedings of the 15th Annual Meeting of ISMRM, Berlin, Germany, 2007. p. 1632.
40. Hernando D, Kühn JP, Mensel B, et al. R2* estimation using “in-phase” echoes in the presence of fat: the effects of complex spectrum of fat. *J Magn Reson Imaging*. 2013;37:717–726.
41. Hernando D, Reeder SB. System and method for magnetic resonance imaging water-fat separation with full dynamic range using in-phase images. US8,957,681B2. 2015.
42. Pineda AR, Reeder SB, Wen Z, Pelc NJ. Cramér-Rao bounds for three-point decomposition of water and fat. *Magn Reson Med*. 2005;54:625–635.
43. Yu H, Reeder SB, McKenzie CA, et al. Single acquisition water-fat separation: feasibility study for dynamic imaging. *Magn Reson Med*. 2006;55:413–422.
44. Hernando D, Sharma SD, Aliyari Ghasabeh M, et al. Multisite, multivendor validation of the accuracy and reproducibility of proton-density fat-fraction quantification at 1.5T and 3T using a fat-water phantom. *Magn Reson Med*. 2017;77:1516–1524.
45. Hernando D, Sharma SD, Kramer H, Reeder SB. On the confounding effect of temperature on chemical shift-encoded fat quantification. *Magn Reson Med*. 2014;72:464–470.
46. Sudlow C, Gallacher J, Allen N, et al. UK Biobank: an open access resource for identifying the causes of a wide range of complex diseases of middle and old age. *PLoS Medicine*. 2015;12:e1001779.
47. Peterson P, Månsson S. Fat quantification using multiecho sequences with bipolar gradients: investigation of accuracy and noise performance. *Magn Reson Med*. 2014;71:219–229.
48. Irving B, Hutton C, Dennis A, et al. Deep quantitative liver segmentation and vessel exclusion to assist in liver assessment. *MIUA*. 2017. https://doi.org/10.1007/978-3-319-60964-5_58.
49. Bland JM, Altman DG. Measuring agreement in method comparison studies. *Stat Methods Med Res*. 1999;8:135–160.
50. Hernando D, Levin YS, Sirlin CB, Reeder SB. Quantification of liver iron with MRI: state of the art and remaining challenges. *J Magn Reson Imaging*. 2014;40:1003–1021.
51. Yu H, Shimakawa A, McKenzie CA, et al. Phase and amplitude correction for multi-echo water-fat separation with bipolar acquisitions. *J Magn Reson Imaging*. 2010;31:1264–1271.

How to cite this article: Triay Bagur A, Hutton C, Irving B, Gyngell ML, Robson MD, Brady M. Magnitude-intrinsic water-fat ambiguity can be resolved with multipeak fat modeling and a multipoint search method. *Magn Reson Med*. 2019;82:460–475. <https://doi.org/10.1002/mrm.27728>